Physics of Plasmas

RESEARCH ARTICLE | JANUARY 13 2025

Effect of voltage polarity on reaction mechanism of air atmospheric surface dielectric barrier discharge: A numerical study

Jiali Lai ; Chunjing Wang ; Jing Li; Yi Peng; Hancheng Xu ; Kaiyue Gao ; Chuanjie Chen ; Muyang Qian ; Bingyan Dong ; Dezhen Wang

Phys. Plasmas 32, 013503 (2025)
https://doi.org/10.1063/5.0238337

Effect of voltage polarity on reaction mechanism of air atmospheric surface dielectric barrier discharge: A numerical study

Cite as: Phys. Plasmas **32**, 013503 (2025); doi: 10.1063/5.0238337
Submitted: 11 September 2024 · Accepted: 12 December 2024 ·
Published Online: 13 January 2025

Jiali Lai,[1] Chunjing Wang,[1] Jing Li,[1] Yi Peng,[1] Hancheng Xu,[1] Kaiyue Gao,[1] Chuanjie Chen,[2] Muyang Qian,[1,a)] Bingyan Dong,[3,a)] and Dezhen Wang[4]

AFFILIATIONS

[1]School of Physics and Materials Science, Nanchang University, Nanchang 330031, China
[2]School of Information Engineering, Yancheng Institute of Technology, Yancheng 224051, China
[3]School of Resources and Environmental Engineering, Jiangxi University of Science and Technology, Ganzhou 341000, China
[4]School of Physics, Dalian University of Technology, Dalian 116024, China

[a)]**Authors to whom correspondence should be addressed:** qianmuyang@ncu.edu.cn and dongbingyan1@sina.com

ABSTRACT

This study establishes a two-dimensional fluid model of nanosecond surface dielectric barrier discharge (nSDBD) at atmospheric air to investigate the effects of positive and negative sinusoidal nanosecond pulsed voltages on the discharge characteristics. Key discharge parameters are studied, including discharge current, distribution of major active particles, surface charge distribution on the dielectric, energy deposition density distribution, and gas temperature. The numerical simulation results indicate that the plasma streamers excited by positive and negative bipolar pulses exhibit markedly different discharge characteristics, with the discharge characteristics in the first half-cycle largely determining those of the entire cycle. Positive bipolar pulsed streamer discharges exhibit greater discharge currents and stronger local electric fields, with faster propagation speeds but also more pronounced declines. The energy deposition of positive bipolar pulse is higher than that of negative bipolar pulse. The discharges driven by negative bipolar pulses exhibit a more pronounced temperature rise effect, primarily due to their higher efficiency in converting electrical energy into thermal energy, leading to stronger localized thermal release. Consequently, the pressure waves generated by negative bipolar pulsed discharges are more intense. These numerical simulation data provide theoretical explanations and references for understanding and optimizing the physical mechanisms of nSDBD.

I. INTRODUCTION

Surface dielectric barrier discharge (SDBD) technology is widely used in various fields, including air purification,[1,2] ozone generation,[3] airflow control,[4–6] and plasma-assisted ignition and combustion.[7–9] In air purification, non-thermal plasma technology utilizes the temperature difference between electrons and gas molecules to generate highly reactive species through strong electric field ionization, effectively treating air pollutants.[1] In airflow control, pioneering experiments using atmospheric nanosecond surface dielectric barrier discharge (nSDBD) for flow control can be traced back to the early 2000s.[10,11] By inducing body force effects through electromagnetic fields or localized heat release, nSDBD technology can reshape flow field structures, adjust wall pressure and shear stress distribution, achieve drag reduction, lift enhancement, precise shock wave control, boundary layer separation, and transition control.[4,12,13] Additionally, in plasma-assisted combustion, nSDBD technology significantly reduces ignition time through rapid radical generation and high-energy state thermal relaxation, demonstrating high-efficiency combustion assistance.[8,14,15] In SDBD, nanosecond pulsed-driven discharges exhibit significant advantages in uniformity, energy efficiency, and chemical activity. However, due to the complexity and dynamics of nanosecond pulsed discharges under high-speed flow conditions, stringent requirements are imposed on the reliability, stability, and energy efficiency of the technology. Thus, numerical simulation becomes crucial for establishing theoretically self-consistent plasma discharge models that reflect experimental results.

To describe the physical characteristics of nSDBD, extensive experimental and numerical simulation studies have been conducted.

For instance, Soloviev *et al.*[16,18] and Soloviev and Krivtsov[17] thoroughly analyzed the excitation and propagation of nanosecond surface streamers. Their research found that diffuse and uniform negative streamers are mainly located a few micrometers near the dielectric, characterized by a locally strong electric field and low electron density, while positive streamers have a strong electric field thickness of tens of micrometers. Additionally, the energy deposition of negative streamers is mainly concentrated near the exposed electrode (cathode), whereas the energy deposition of positive streamers is almost uniformly distributed along the streamer propagation. Corke *et al.*[19] and Little *et al.*[20] provided an overview of AC SDBD actuators applied to airflow control, discussing in detail the electrical and mechanical characteristics of SDBD. Ren *et al.*[21] used a two-dimensional (2D) fluid model to study the impact of residual surface charges on the characteristics of repetitive nSDBD discharges at atmospheric pressure. Under bipolar mode, residual charges with polarity opposite to the exposed pulse enhance SDBD, while in unipolar mode, they suppress the discharge. The study in Ref. 22 investigated the effects of SDBD plasma actuators driven by nanosecond pulses of both positive and negative polarity. The results demonstrate that under equivalent conditions, negative polarity pulses are capable of generating stronger pressure waves and more efficiently transferring electrical energy into the near-surface gas in the form of heat. Babaeva *et al.*[23] revealed significant differences between positive and negative polarity nSDBD through 2D fluid and fluid-Monte Carlo simulations. Zhu and Starikovskaia[24] studied the physical mechanism of fast gas heating (FGH) in atmospheric pressure air nSDBD. They discussed the local field approximation for simplified kinetic nSDBD modeling, revealing the energy distribution of FGH and its impact on gas temperature, and evaluated the roles of different reactions in fluid dynamic disturbances. Zhang *et al.*[25] used a 2D fluid model to simulate the impact of pulse voltage amplitude and polarity on nSDBD discharge, mainly exploring the dynamics of streamers, pressure waves, and vortices. The results indicated that pressure waves are formed by rapid gas heating induced by pulsed discharges, while the generation and development of vortices are attributed to the ion wind produced by the plasma (EHD effect).

The spatiotemporal evolution characteristics of nSDBD have also been extensively studied experimentally.[11,26,27] Stepanyan *et al.*[28] experimentally investigated the development and evolution of 1–6 bars atmospheric air nSDBD. The discharge evolves into a set of streamers that start simultaneously from the exposed electrode and propagate along the dielectric layer, forming a "quasi-uniform" plasma layer, with streamer filaments observed a few nanoseconds after discharge initiation. Peng *et al.*[29] combined experimental diagnostics and numerical simulation to study the dynamic evolution and discharge mode transition of repetitive pulse-driven three-electrode SDBD, aiming to better control plasma modes and optimize applications. Qian *et al.*[30] conducted experimental characterization of an atmospheric plasma jet with a coaxial mesh cylindrical electrode design. The study investigated the impact of gas flow rate on the length of the plasma jet, revealing that the plasma jet exhibited three distinct modes depending on the gas flow rate. The behavior of nSDBD under exposure was independently examined.[31,32] The transition from streamers to filaments was analyzed in single-pass experiments with various gas mixtures. The findings revealed that continuous wavelength emissions are concentrated in a narrow near-axis region originating from the filaments. In filamentary mode, exposed electrode needle–ring plasma discharge plasma and nSDBD plasma exhibit similar plasma characteristics. Zhang *et al.*[33] combined experimental and numerical simulations to study the spatiotemporal dynamics of positive and negative streamers in a pin-to-plate volume DBD. They found that the spatial propagation of positive streamers depends on the electron avalanches induced by photoelectrons ahead of the streamer head, whereas negative streamers behave differently, revealing an interesting phenomenon of floating positive surface discharge. Shcherbanev *et al.*[34] experimentally investigated the plasma characteristics of filamentary nSDBD, considering the effects of pressure and voltage on current, deposited energy, electron density, and electron temperature, discussing and explaining plasma characteristics in filamentary nanosecond discharges and the role of excited species in the transition from streamer to filamentary discharge.

Although previous research has extensively studied the mechanisms of atmospheric air nSDBD and achieved original findings, these studies primarily focused on the effects of pressure, surface charge deposition, and rapid gas heating on discharge characteristics. The streamer discharges excited by the single sinusoidal voltage pulse with starting positive or starting negative voltage half-cycle are studied in detail. The main challenge is how to experimentally generate a fast sine pulse (with a period of 20 ns) with either a starting positive or negative half-cycle first. Assuming this issue can be addressed, a direct comparison between numerical simulation and experimental diagnostic can be conducted, focusing on aspects such as the measured and calculated current waveform, radius, and velocity of the discharge front, 2D map of $N_2(C^3\prod_u) \rightarrow N_2(B^3\prod_g)$ emission, etc. Therefore, this paper aims to systematically explore the characteristics of atmospheric pressure air nSDBD under positive and negative sinusoidal pulse excitation through numerical simulations. The results show that the polarity of the pulse voltage in the first half-cycle significantly affects the nSDBD discharge characteristics in the second half-cycle and even determines the entire pulse discharge dynamics. This study examines key discharge parameters, including discharge current, spatiotemporal distribution of particle density, electric field characteristics, surface charge evolution, energy deposition distribution, gas temperature, and pressure waves, to reveal the effects of positive and negative sinusoidal nanosecond pulse voltage polarity on the plasma dynamics and physical mechanisms of atmospheric pressure air nSDBD.

II. MODEL DESCRIPTION

The fluid modeling of SDBD is based on the PASSKEy code.[35] PASSKEy is a parallel streamer-plasma coupled solver developed in Fortran90. Detailed numerical methods and benchmarks can be found in Ref. 24. This section briefly introduces the governing equations, boundary conditions, computational domain, and chemical reactions of our model.

A. Governing equations

The particle continuity equations under the drift-diffusion approximation are as follows:

$$\frac{\partial n_i}{\partial t} + \nabla \cdot \mathbf{\Gamma_i} = S_i + S_{ph}, i = 1, 2, \ldots, N_{total}, \quad (1)$$

$$\mathbf{\Gamma_i} = -D_i \nabla n_i - \left(\frac{q_i}{|q_i|}\right) \mu_i n_i \nabla \phi, i = 1, 2, \ldots, N_{charge}, \quad (2)$$

$$\frac{\partial(n_e\varepsilon_m)}{\partial t} + \nabla\cdot\mathbf{\Gamma_\varepsilon} = -|q_e|\cdot\mathbf{E}\cdot\mathbf{\Gamma_e} - P(\varepsilon_m), \tag{3}$$

$$\mathbf{\Gamma_\varepsilon} = -D_\varepsilon\nabla(n_e\varepsilon_m) - n_e\varepsilon_m\mu_\varepsilon\mathbf{E}, \tag{4}$$

where n_i, q_i, $\mathbf{\Gamma}_i$, S_i, D_i, and μ_i are the number density, charge, flux, source term due to gas-phase reactions, diffusion coefficient, and mobility of species i, respectively. S_{ph} is the photoionization source term. n_e, q_e, ε_m, $\mathbf{\Gamma}_\varepsilon$, D_ε, and μ_ε are the electron number density, elementary charge, mean electron energy, electron energy flux, electron energy diffusion coefficient, and mobility, respectively. $\mathbf{E}$ is the electric field. The electron transport coefficients, reaction rates, and electron collision power loss $P(\varepsilon_m)$ are calculated by Bolsig+[36] by solving the Boltzmann equation. The cross-section data related to N_2 comes from the SIGLO database[37] and Ref. 38, while the cross-section data related to O_2 comes from the PHELPS database[39] and Ref. 40. In fluid modeling, the local mean energy approximation (LMEA) is relatively time-consuming, while the local field approximation (LFA) may result in accuracy loss. In the ionization region, LFA may lead to an underestimation of ionization, while in the near-wall region close to the medium's surface, LFA may cause an overestimation of ionization.[24] To ensure calculation accuracy, this study uses the LMEA method for computational analysis.

The photoionization source term for electrons and O_2^+ is calculated by the three-exponential Helmholtz equation in air, assuming that the ionization of oxygen molecules is induced by radiation photons from excited nitrogen molecules[41]

$$S_{ph} = \sum_j S_{ph}^j, \tag{5}$$

$$\nabla^2 S_{ph}^j - \left(\lambda_j p_{O_2}\right)^2 S_{ph}^j = -A_j p_{O_2}^2 I, \tag{6}$$

$$I = \xi\frac{P_q}{P+P_q}\alpha\mu_e E n_e, \tag{7}$$

where p_{O_2} is the partial pressure of O_2, taken as 152 Torr.[42] I is the ionization source rate. α is the Townsend ionization coefficient. P is the ambient pressure. $\mu_e E$ is the absolute drift velocity of electrons, and n_e is the density of electrons. P_q is a quenching pressure of $N_2(C^3\Pi_u)$, taken as 30 Torr.[43] λ_j and A_j are fitting parameters of the photoionization function, taken from Ref. 42. The specific values are shown in Table I.

The particle continuity equation and the electron energy conservation equation are closed by the Poisson equation of the electrostatic field. The solution of the Poisson equation takes into account the surface charge density on the dielectric

$$\nabla(\varepsilon_0\varepsilon_r\nabla\phi) = -\rho - \sigma, \tag{8}$$

$$\frac{\partial\sigma}{\partial t} = \sum_i q_i(-\nabla\cdot\mathbf{\Gamma_i}), \tag{9}$$

TABLE I. Coefficients of the three terms Helmholtz equation A_j and λ_j.

j	A_j ($\mathrm{cm^{-2}\,Torr^{-1}}$)	λ_j ($\mathrm{cm^{-1}\,Torr^{-1}}$)
1	1.986×10^{-4}	0.0553
2	0.0051	0.1460
3	0.4886	0.89

where ε_0 is the vacuum permittivity, ε_r is the relative dielectric constant, ρ is the space charge density, σ is the surface charge density on the dielectric, and ϕ is the electric potential.

B. Boundary conditions

For the Poisson equation, classical Dirichlet boundary conditions are applied on metal surfaces: $\phi = U(t)$, while Neumann boundary conditions are used on nonmetal boundaries: $\partial\phi/\partial n = 0$, n is the normal vector pointing outward. At each time step, the charge flux toward the dielectric boundaries in the plasma region is collected. Surface charges accumulate on the dielectric surfaces, stored at the edges of finite volume mesh cells, and considered as additional charges when solving the Poisson equation. For the Helmholtz equation, boundary conditions $S_{ph} = 0$ are set at the domain boundaries far from the plasma region.

For the transport equations, incoming electrons at the boundary are represented by $\partial\mathbf{\Gamma}_e/\partial n = 0$, and outgoing electrons are represented by $\mathbf{\Gamma}_e = -\gamma\mathbf{\Gamma}_i$. Incoming ions at the boundary are represented by $\partial\mathbf{\Gamma}_i/\partial n = 0$, and outgoing ions are represented by $\mathbf{\Gamma}_i = 0$. In particular, for the thin high electric field layer formed above the dielectric surface in SDBD driven by negative pulse, it is necessary to take into account the plasma sheath contribution to the electron flux on the dielectric surface. More detailed and refined physical boundary conditions can be found in Refs. 44 and 45. The model assumes a secondary emission coefficient of $\gamma = 0.01$ for both metals and dielectrics. Since the photoionization source in the air exceeds the secondary emission from the surface, this value will not significantly affect the evolution of the discharge.[42] Based on empirical data, the recommended range for γ is between 0.01 and 0.05,[42] so γ is set to be 0.01 in our model.

C. Computational domain and chemical reactions

A 2D computational domain of 3.0×1.0 cm is shown in Fig. 1(a). The exposed metal electrode (red area) has a thickness of 0.05 mm, and the material has a density of 8500 $\mathrm{kg/m^3}$. The ground

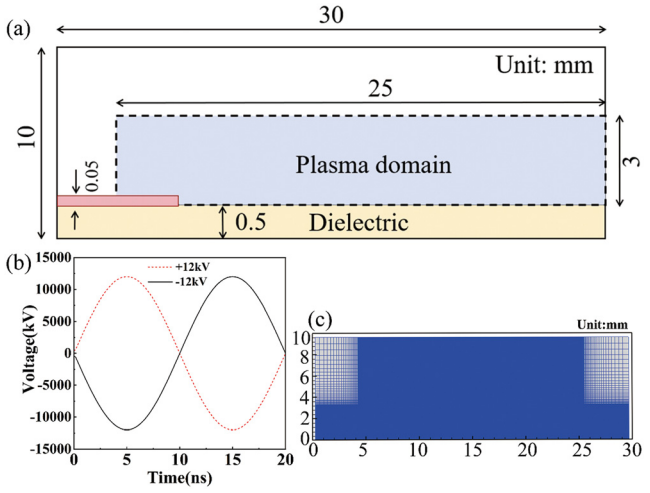

FIG. 1. (a) Simulated geometric structure diagram, (b) sinusoidal pulse waveform with a peak of +12 kV and −12 kV, and a period of 20 ns, and (c) model mesh segmentation diagram.

electrode (dielectric bottom layer) has negligible thickness. A dielectric layer with a thickness of 0.5 mm ($\varepsilon = 4$) separates the two electrodes, and the density of the dielectric material is 1420 kg/m^3. The discharge is conducted at an initial temperature of 300 K and standard atmospheric pressure, with the boundaries of the computational domain set to be insulated and have zero charge. Since a computational domain that is too narrow can affect the development of the discharge, the domain width should be sufficiently large. However, considering the degrees of freedom in the model calculation, the computational domain cannot be too large either. Therefore, in this paper, the width of the plasma region is set to 2.5 cm. A sinusoidal pulse waveform is applied to the exposed electrode

$$\phi = U_0 \sin(2\pi f t). \tag{10}$$

The applied peak voltage U_0 is +12 kV in positive bipolar mode and −12 kV in negative bipolar mode, with a frequency f of 50 MHz, as shown in Fig. 1(b). The lower dielectric plate is grounded.

Due to the high electron collision frequency at atmospheric pressure, the accuracy and efficiency of numerical simulation results are greatly influenced by the finite element mesh division. Generally, the finite element mesh in non-equilibrium atmospheric plasma is very fine, with a mesh scale in the micrometer range, especially in the sheath region near the anode and dielectric plate, requiring even finer mesh. As shown in Fig. 1(c), the computational domain is discretized using a square mesh. The mesh in the plasma computational region is set to 8 μm, with further mesh refinement near the initial filament appearance and the dielectric surface where the surface streamers propagate. Horizontally, starting from the right end of the exposed electrode to a range of 2.0 cm, a 4 μm square mesh is used. Vertically, from 0.02 mm below the dielectric plate to 0.2 mm above the dielectric plate, a 3 μm square mesh is used.

To facilitate calculations, a simplified air chemical reaction model is used. The N_2/O_2 kinetic scheme includes 38 chemical reactions and 15 species: the particles included in the plasma model are listed in Table II, and the considered chemical reactions are shown in Table III.[24]

III. RESULTS AND DISCUSSION

A. Volt–ampere characteristics

Figures 2(a) and 2(b) show the volt–ampere characteristics of single sinusoidal pulses at +12 kV and −12 kV, respectively. The discharge current and the applied voltage exhibit similar trends, with two consecutive discharge current pulses occurring in each cycle.[30] Clearly, the current in the first positive half-cycle of the positive bipolar pulse [Fig. 2(a)] is significantly higher than the current in the first negative half-cycle of the negative bipolar pulse [Fig. 2(b)]. This is because, during negative jet propagation, the ionization rate caused by photoionization is two orders of magnitude lower than that caused by electron impact ionization, making photoionization negligible.[49–51] In contrast, positive streamers have photoionization that creates a source of free electrons, leading to higher conductivity and larger current. In addition, the gas breakdown in the first positive half-cycle of the positive bipolar pulse occurs at around 1.2 ns, with the corresponding electrode voltage being approximately 4400 V. However, the gas breakdown in the first negative half-cycle of the negative bipolar pulse occurs at around 0.35 ns, with the corresponding electrode voltage being approximately 1300 V. The breakdown voltage of the positive bipolar pulse is significantly higher than that of the negative bipolar pulse, which is generally consistent with the experimental results in Ref. 52. During the first positive half-cycle of the positive bipolar pulse, a large number of positive charges accumulate on the dielectric surface, inhibiting the drift of electrons toward the exposed electrode, resulting in a decrease in current. Conversely, during the first negative half-cycle of the negative bipolar pulse, many electrons accumulate on the dielectric surface, inhibiting subsequent electron drift, also leading to a decrease in current.[18] This is manifested in a decrease in current around 3.0 ns, as shown in Fig. 2. Whether it is a positive bipolar or negative bipolar pulse, the current peaks are around 3.0 and 12.5 ns.

The change in current polarity around 7.0 ns before the end of the first half-cycle indicates the occurrence of reverse breakdown. This phenomenon is primarily due to the reduction in the applied voltage during the falling edge of the pulse, which causes the built-in electric field formed by the accumulated charges on the dielectric surface to significantly exceed the applied electric field, leading to reverse breakdown.[18] After 10 ns, the voltage polarity reverses, and the applied electric field aligns with the built-in field, enhancing the electric field. This increases the reverse breakdown current, forming a discharge channel through which electrons quickly neutralize the deposited charges from the first half-cycle, causing the current to decrease. When the pulse reaches the falling edge after 15 ns, the applied electric field decreases, and large opposite charges accumulate on the dielectric surface. The built-in electric field formed by these surface charges again exceeds the applied electric field, resulting in a second reversal of current around 17 ns.

TABLE II. Table of species included in the model.

Electron	e
Molecule	N_2, O_2
Ion	N_2^+, N_4^+, O_2^+, O_4^+, O^-, O_2^-, $O_2^+N_2$
Radical	O
Excited-state particles	$N_2(A^3\Sigma_u)$, $N_2(B^3\Pi_g)$, $N_2(C^3\Pi_u)$, O(1D)

B. Streamer evolution mechanism

Figures 3(a) and 3(b) show the spatiotemporal distribution of electron density in streamer discharges under two types of pulses. For comparison, both figures use the same color scale. As shown, the discharge behavior is closely related to the polarity of the exposed electrode. For the positive bipolar polarity, the first half-cycle exhibits a concentrated positive streamer propagating from the anode to the cathode. In contrast, the subsequent half-cycle, due to the reversal of the voltage polarity, forms a negative streamer moving from the cathode to the anode, resulting in a more diffuse and uniform discharge at the electrode.[23,25] Conversely, under negative bipolar pulse, the first half-cycle displays a diffuse and uniform negative streamer propagating from the cathode to the anode, while the subsequent half-cycle, with the reversed voltage polarity, forms a concentrated positive streamer moving from the anode to the cathode.[30] It is evident that the discharge in the first half-cycle significantly influences the discharge in the second half-cycle, primarily due to the memory effect caused by the residual charges on the dielectric surface.

To compare the emission characteristics of specific molecules under two types of pulses, it is necessary to understand their electron

TABLE III. Table of chemical reactions included in the model. Note: The units for the reaction rate constants of bimolecular collisions are $m^3 \cdot s^{-1}$; the units for the reaction rate constants of termolecular collisions are $m^6 \cdot s^{-1}$; and the unit for Te is K.

No.	Reaction	Rate constant	Refs.
R1	$e + N_2 \rightarrow N_2^+ + e + e$	$f(\varepsilon_m)$	37,38
R2	$e + O_2 \rightarrow O_2^+ + e + e$	$f(\varepsilon_m)$	39,40
R3	$e + N_2 \rightarrow e + N_2(A^3\sum_u)$	$f(\varepsilon_m)$	37,38
R4	$e + N_2 \rightarrow e + N_2(B^3\prod_g)$	$f(\varepsilon_m)$	37,38
R5	$e + N_2 \rightarrow e + N_2(C^3\prod_u)$	$f(\varepsilon_m)$	37,38
R6	$e + O_2 \rightarrow e + O + O$	$f(\varepsilon_m)$	39,40
R7	$e + O_2 \rightarrow e + O + O(^1D)$	$f(\varepsilon_m)$	39,40
R8	$e + O_2 \rightarrow O^- + O$	$f(\varepsilon_m)$	39,40
R9	$N_2^+ + N_2 + N_2 \rightarrow N_4^+ + N_2$	5.0×10^{-41}	46,47
R10	$N_2^+ + N_2 + O_2 \rightarrow N_4^+ + O_2$	5.0×10^{-41}	46,47
R11	$N_4^+ + O_2 \rightarrow O_2^+ + N_2 + N_2$	2.5×10^{-16}	46,47
R12	$N_2^+ + O_2 \rightarrow O_2^+ + N_2$	6.0×10^{-17}	46,47
R13	$O_2^+ + N_2 + N_2 \rightarrow O_2^+N_2 + N_2$	9.0×10^{-43}	47
R14	$O_2^+N_2 + N_2 \rightarrow O_2^+ + N_2 + N_2$	4.3×10^{-16}	47
R15	$O_2^+N_2 + O_2 \rightarrow O_4^+ + N_2$	1.0×10^{-15}	47
R16	$O_2^+ + O_2 + N_2 \rightarrow O_4^+ + N_2$	2.4×10^{-42}	46,47
R17	$O_2^+ + O_2 + O_2 \rightarrow O_4^+ + O_2$	2.4×10^{-42}	46,47
R18	$e + O_2 + O_2 \rightarrow O_2^- + O_2$	$2.0 \times 10^{-41}(300/(T_e + 1))$	47
R19	$O^- + O \rightarrow O_2 + e$	1.4×10^{-16}	48
R20	$O_2^- + O \rightarrow O_2 + O + e$	1.5×10^{-16}	48
R21	$e + N_4^+ \rightarrow N_2 + N_2(C^3\prod_u)$	$2.3 \times 10^{-12}(300/T_e)^{0.53}$	48
R22	$e + N_2^+ \rightarrow N + N$	$1.8 \times 10^{-13}(300/T_e)^{0.39}$	48
R23	$e + O_4^+ \rightarrow O + O + O_2$	$1.4 \times 10^{-12}(300/(T_e + 1))^{0.5}$	46,47
R24	$e + O_2^+ \rightarrow O + O$	$2.0 \times 10^{-13}(300/(T_e + 1))$	46,47
R25	$O_2^- + O_4^+ \rightarrow O_2 + O_2 + O_2$	1.0×10^{-13}	47
R26	$O_2^- + O_4^+ + N_2 \rightarrow O_2 + O_2 + O_2 + N_2$	2.0×10^{-37}	47
R27	$O_2^- + O_4^+ + O_2 \rightarrow O_2 + O_2 + O_2 + O_2$	2.0×10^{-37}	47
R28	$O_2^- + O_2^+ + N_2 \rightarrow O_2 + O_2 + N_2$	2.0×10^{-37}	47
R29	$O_2^- + O_2^+ + O_2 \rightarrow O_2 + O_2 + O_2$	2.0×10^{-37}	47
R30	$O^- + N_2^+ \rightarrow O + N + N$	$2.0 \times 10–13(300/T_{gas})^{0.5}$	47
R31	$N_2(C^3\prod_u) + N_2 \rightarrow N_2(B^3\prod_g) + N_2$	1.3×10^{-17}	46
R32	$N_2(C^3\prod_u) + O_2 \rightarrow N_2 + O + O(^1D)$	3.0×10^{-16}	46
R33	$N_2(C^3\prod_u) \rightarrow N_2(B^3\prod_g)$	2.45×10^7	47
R34	$N_2(B^3\prod_g) + O_2 \rightarrow N_2 + O + O$	3.0×10^{-16}	46
R35	$N_2(B^3\prod_g) + N_2 \rightarrow N_2(A^3\sum_u) + N_2$	1.0×10^{-17}	46
R36	$N_2(A^3\sum_u) + O_2 \rightarrow N_2 + O + O$	$2.5 \times 10^{-18}(T_{gas}/300)^{0.5}$	46
R37	$O(^1D) + O_2 \rightarrow O + O_2$	$3.3 \times 10^{-17}\exp(67/T_{gas})$	46
R38	$O(^1D) + N_2 \rightarrow O + N_2$	$1.8 \times 10^{-17}\exp(107/T_{gas})$	46

density and electric field characteristics in detail. The reduced electric field evolution for positive and negative bipolar pulses is shown in Fig. 4, where the maximum electric field at the streamer head at 5 ns corresponds to approximately 1000 Td. It can be observed that in the first half-cycle, the propagation direction of the positive bipolar streamer is opposite to the electron drift direction, with an extremely strong electric field at the streamer head. In contrast, the propagation direction of the negative bipolar streamer is consistent with the electron drift direction, with the electric field primarily concentrated near the streamer front,[23] and the electric field intensity at the negative streamer front is much lower than that of the positive streamer.

Figure 5 shows the maximum reduced electric field and propagation speed of positive and negative bipolar pulsed streamers. The propagation distance is determined by locating where the electric field at the streamer head reaches its maximum value, thus calculating the propagation speed. For both types of pulses, the peak streamer speed occurs in the 3–4 ns interval, as the applied voltage starts to decrease after 5 ns, reducing the electric field intensity. Initially, the streamer

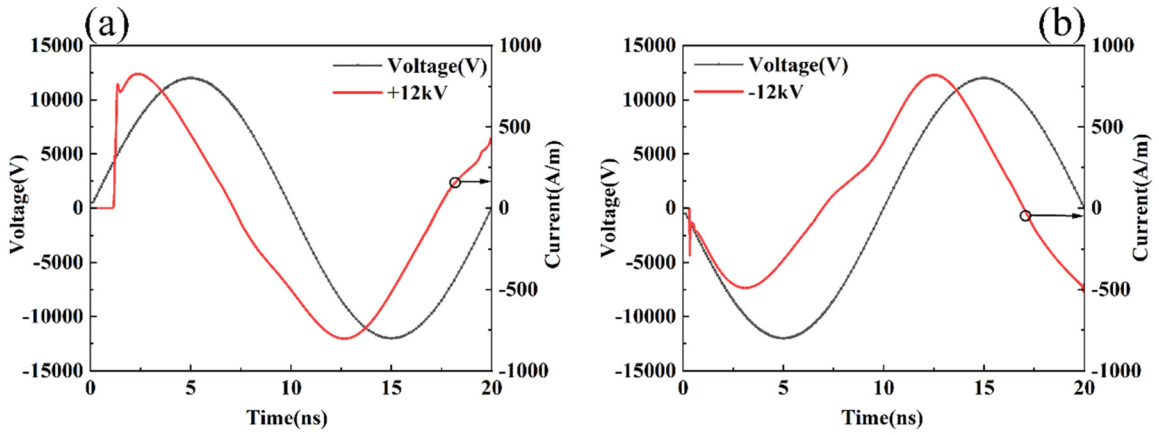

FIG. 2. Volt–ampere characteristics curve of (a) +12 kV pulse discharge (positive bipolar pulse) and (b) −12 kV pulse discharge (negative bipolar pulse).

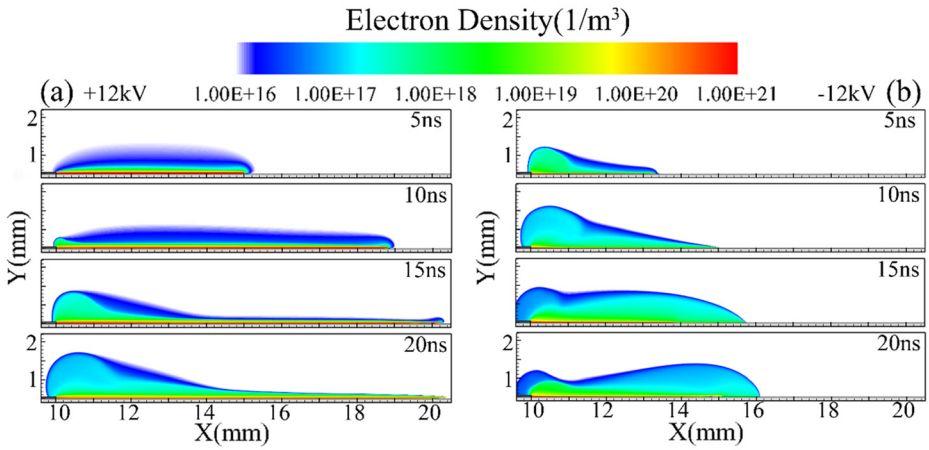

FIG. 3. Spatiotemporal distributions of electron density for (a) positive and (b) negative bipolar pulsed streamers.

accelerates rapidly, reaching speeds of 10^5 m/s, with the positive bipolar pulsed streamer even peaking at 10^6 m/s, then gradually decelerates until it stops propagating. The maximum field strength at the head of positive streamer is significantly higher than that of negative streamer, which results in the propagation speed of the positive streamer being higher most of the time.

These phenomena are determined by the differences in the propagation mechanisms of positive and negative streamers.[18,26] In a negative streamer, electrons released from the cathode migrate to and accumulate significantly on the dielectric surface. In contrast, in a positive streamer, electrons migrate against the direction of the streamer propagation toward the exposed anode, accelerating in response to the

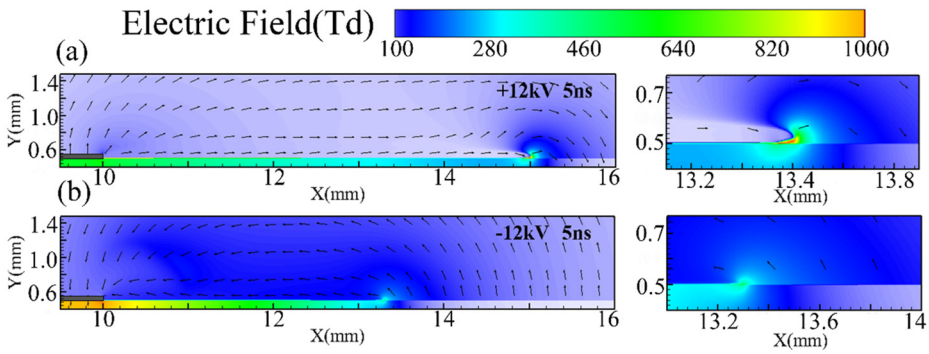

FIG. 4. Reduced electric field for (a) positive and (b) negative bipolar pulsed streamers.

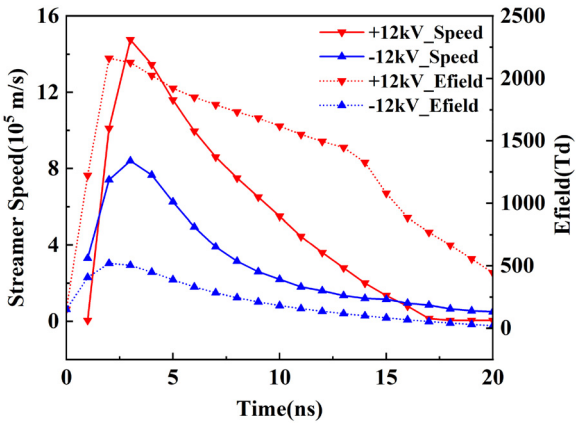

FIG. 5. Electric field intensity and propagation speed for positive bipolar and negative bipolar pulsed streamers.

electric field while losing energy through collisions with neutral gas molecules, with ions remaining nearly stationary. Consequently, the formation mechanisms of positive and negative streamers differ markedly.

The positive space charge at the head of the positive streamer leads to a very strong electric field between the streamer head and the dielectric, forming a high field strength region with a thickness of approximately 20–30 μm. Above this region, the electric field strength rapidly weakens. Although a high-field region also forms at the tip of the negative streamer, its field strength is lower than that of the positive streamer, resulting in the higher propagation speed of the positive streamer. Another important factor is that photoionization during the propagation of negative streamers can be neglected, whereas positive streamers generate seed electrons through photoionization to compensate for the rapid loss of electrons. As a result, the conductivity of negative streamers is relatively low. This lower conductivity leads to a greater voltage drop within the discharge channel, resulting in a lower voltage at the head of the negative streamer.[53] As shown in Fig. 5, over a short period, the propagation speed of the positive bipolar pulsed streamer decreases faster, even dropping below that of the negative bipolar pulsed streamer by the end of the pulse. This is because the positive bipolar streamer accumulates more positive charges on the dielectric surface, weakening the applied electric field and inhibiting the advance of the streamer. When the pulse voltage starts to decrease or even reverse, the effect of the surface charges becomes significantly stronger, leading to a more pronounced decrease in the speed of the positive bipolar streamer.

Studies have shown that the light intensity of streamer discharge is directly linearly correlated with the high-energy excitation state of nitrogen molecules $N_2(C^3\Pi_u)$ distribution.[54] Therefore, Fig. 6 presents a 2D spatiotemporal distribution map of the $N_2(C^3\Pi_u)$ number density. Two significant characteristic regions were observed: one is a strong light intensity region located at the streamer head, and the other is a similar region adjacent to the exposed electrode. As time progresses, the strong light intensity in these two regions gradually separates spatially, until around 15 ns or longer, when the light intensity between the streamer head and the near-electrode region nearly disappears. This visually reflects the reconstruction and dissipation process of the electric field on the spatiotemporal scale. In the case of negative bipolar, the initial light intensity distribution (around 5 ns) is similar to the electron density distribution. Subsequently (around 10 ns), the light intensity tends to flatten on the dielectric surface. After the electrode polarity reverses, the light intensity gradually increases (corresponding to 15 ns), which is related to the enhanced electric field in the streamer channel above the dielectric due to the reverse voltage increase. As the voltage decreases, the light emission on the dielectric surface flattens again. These observed phenomena are consistent with the report in Ref. 53.

C. Surface charge and energy deposition

Figure 7 shows the spatial and temporal evolution of surface charges on the dielectric under two types of pulses. The distribution of surface charges reflects the trajectory of the streamers. The polarity of the surface charge is consistent with the polarity of the applied voltage pulse. During the first half-cycle of a +12 kV sinusoidal pulses, positive charges accumulate on the dielectric surface. As the streamers propagate and the voltage polarity reverses in the second half-cycle, the surface charges gradually neutralize. However, at the end of the pulse, positive charges remain on the dielectric surface, especially at the streamer front. Obviously, under positive bipolar pulse, whether in the positive pulse of first half-cycle or the negative pulse of second half-cycle, the streamer propagation distance is significantly longer than

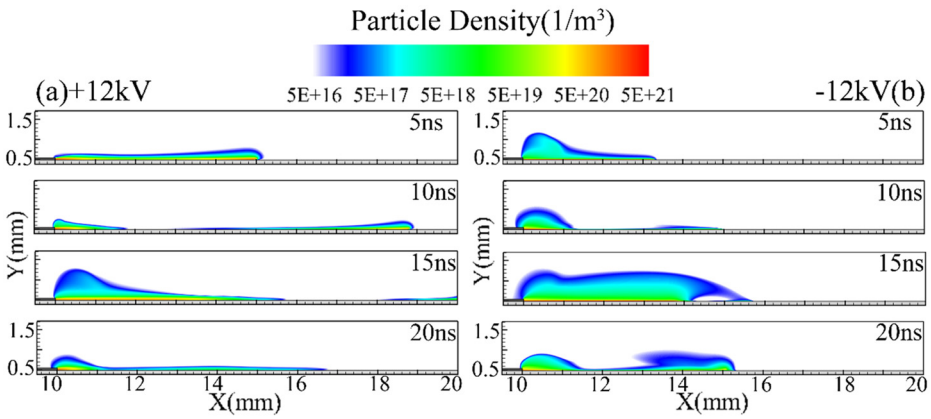

FIG. 6. $N_2(C^3\prod_u)$ radical density of (a) positive and (b) negative bipolar pulsed streamers.

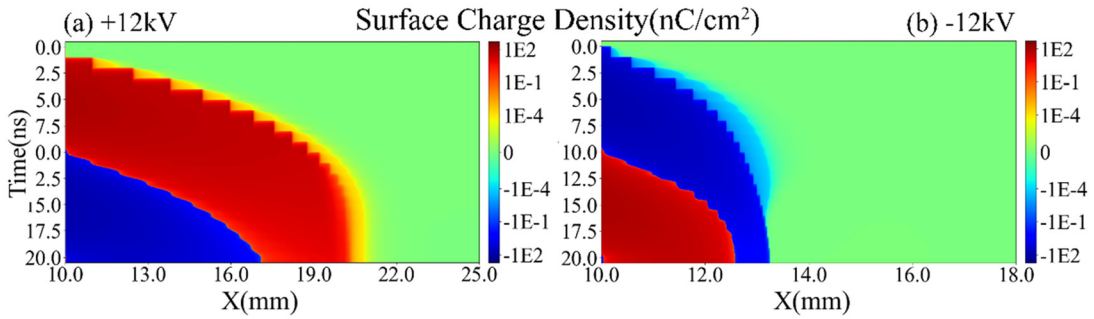

FIG. 7. Temporal and spatial evolution of surface charges on the dielectric under (a) positive and (b) negative bipolar pulsed streamers.

that under negative bipolar pulse. This suggests that the selection of positive and negative pulses in the first half-cycle greatly influences the distribution of residual surface charges on the dielectric, which plays an important role in the nSDBD plasma discharge characteristics.

Figure 8 illustrates the spatial distribution of energy density under two types of pulses at the end of pulse voltage (20 ns). As can be seen, the peak energy density is concentrated near the electrode and gradually decreases along the dielectric surface, as shown in Figs. 8(a) and 8(b). Predictably, the energy coverage in the x-direction is much broader in the positive bipolar mode. The energy density distribution along a 10 μm line above the dielectric is shown in Fig. 8(c). Within the 10–13 μm range, the energy densities of both modes are approximately the same. However, in the 13–25 μm range, the deposited energy density of negative bipolar pulsed streamer is significantly weaker than that of positive bipolar pulsed streamer. Figure 8(d) shows the total energy deposition, calculated by multiplying the energy density by volume of each grid cell and integrating over the entire plasma domain. The results indicate that the total energy under the positive bipolar mode is significantly higher than that under the negative bipolar mode. Studies have shown that higher coupled energy during discharge pulses is associated with more surface charge transfer, consistent with previous experimental observations.[54]

D. Behavior of electric field components

Figure 9 comprehensively illustrates the temporal and spatial evolution of the horizontal (E_x) and vertical (E_y) electric field components during the operation of SDBD under two types of pulses. Measurements were taken at points located 100 μm, 2 mm, and 5 mm from the electrode interface along the x-axis, and 3 μm above the dielectric surface along the y-axis. It was observed that at 100 μm near the electrode, the electric field components first increased to their peak values and then sharply decayed, marking the initial occurrence of breakdown. During the first half of the pulse cycle, as the distance

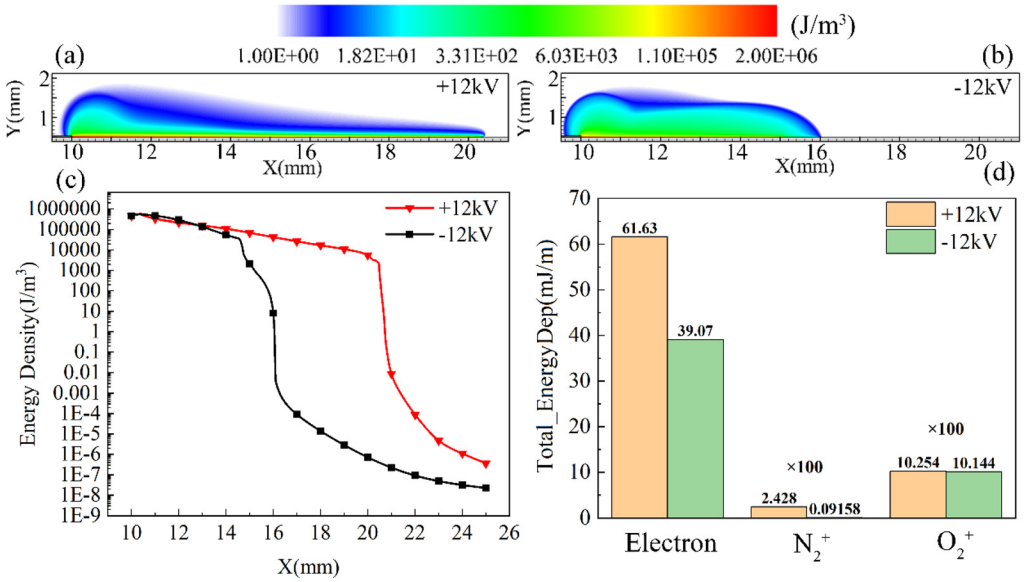

FIG. 8. Spatial distribution of energy density under (a) positive and (b) negative bipolar pulsed streamers at the end of pulse voltage (20 ns), (c) energy density along a 10 μm line above the dielectric, and (d) comparison of total energy deposited in the plasma region between positive bipolar and negative bipolar pulses.

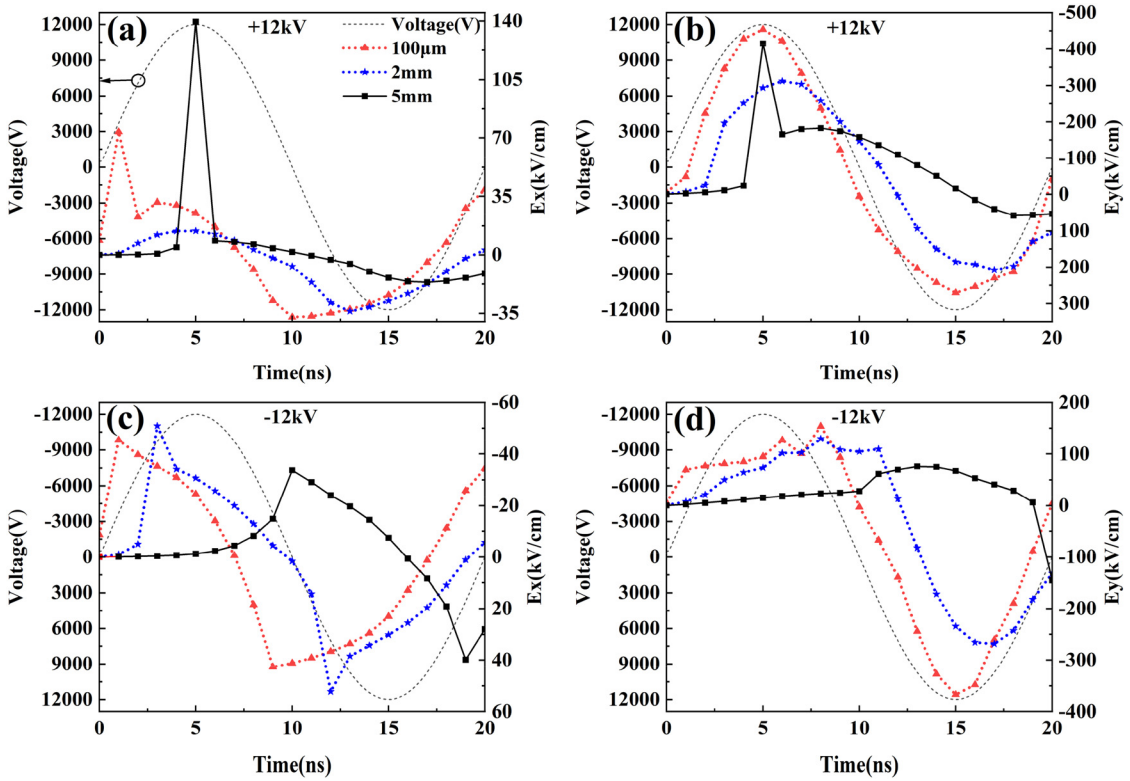

FIG. 9. Time evolution of the electric field vector components for (a) and (b) positive and (c) and (d) negative bipolar pulsed streamers at different positions, the left column represents the horizontal component E_x, and the right column represents the vertical component E_y.

from the exposed electrode increased, the electric field components at 2 and 5 mm sequentially reached their peak values, reflecting the forward propagation of the streamer. Notably, before the critical point of polarity reversal, the E_x-component exhibited signs of reversal for both positive and negative bipolar pulses, indicating the occurrence of reverse breakdown.

In the second half of the pulse period, the electric field components at 100 μm, 2 mm, and 5 mm sequentially reached negative peak values, with subsequent significant declines also indicating breakdown occurrence. Specifically, at 20 ns, for the positive bipolar pulse, the E_x and E_y components near the electrode at 100 μm reversed again, revealing a secondary reverse breakdown phenomenon in the electrode region. For the negative bipolar pulse, besides the aforementioned effects, a reversal in the E_x-component was also observed at 2 mm, indicating a more intense reverse breakdown process under negative bipolar pulse. This conclusion can be indirectly corroborated by the deposition of a small amount of negative surface charge in the exposed electrode area at the end of negative bipolar pulse (as shown in Fig. 7).

Further analysis shows that the E_x and E_y components under negative bipolar pulse exhibited weaker amplitudes compared to the positive bipolar pulse. This difference can be attributed to the unique localized high-field region at the head of the positive streamer, which drives the streamer to form a concentrated shape and develop under the guidance of positive space charges. In contrast, the negative streamer maintains a more dispersed propagation state, developing close to the dielectric surface, resulting in significantly lower

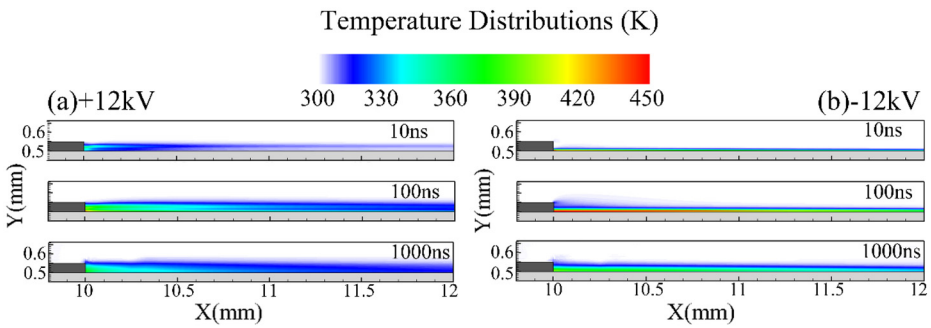

FIG. 10. (a) Spatiotemporal distribution characteristics of temperature for (a) positive and (b) negative bipolar pulsed streamers.

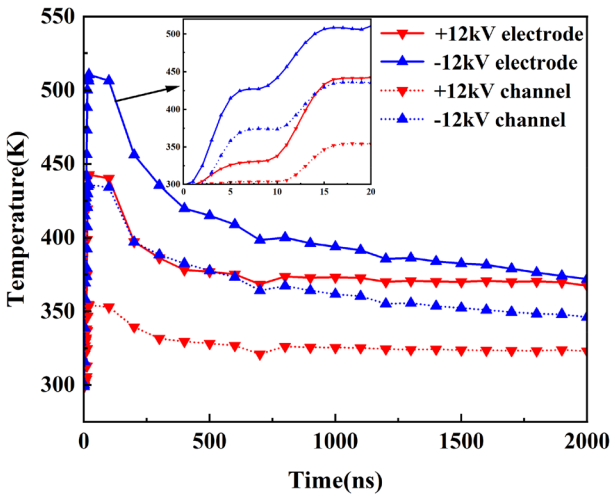

FIG. 11. Gas temperature variations at the electrode and within the channel under two types of pulses.

amplitudes of the E_x and E_y components compared to the positive polarity scenario.

E. Gas temperature and pressure waves

During atmospheric pressure nSDBD discharge, the heat release effect triggered by the interaction between charged particles and excited-state radicals (primarily nitrogen molecule excitations), known as FGH, significantly impacts the temperature within the discharge region.[46] Figures 10(a) and 10(b) illustrate the temperature distributions calculated for 10, 100, and 1000 ns in positive and negative bipolar pulsed streamers. For a more detailed quantitative analysis, this study focuses on two characteristic points: 3 μm above the dielectric surface, 10 μm and 1 mm from the right end of the exposed electrode, tracking the transient temperature changes near the electrode region and within the discharge channel, as shown in Fig. 11. The results indicate that both polarity pulses form distinct heating channels above the dielectric layer, with higher temperatures near the electrode compared to the channel interior. Near the electrode, the peak temperature at negative bipolar conditions reaches 510 K, while under positive bipolar conditions, it is 440 K, suggesting a more pronounced thermal effect of negative polarity pulsed discharge in localized areas.[24] Within the discharge channel, the temperature rise induced by negative bipolar pulse is about 50 K, whereas positive bipolar pulsed discharge can cause a temperature increase of up to 140 K. The more significant temperature rise in positive bipolar pulsed discharge differs from the findings in Ref. 24, likely due to different measurement locations. A point 3 μm above the dielectric surface is selected in this work, while 25 μm above the surface is measured in Ref. 23. The subplot in Fig. 11 reveals that within the first 20 ns of the pulses, the temperature near the electrode (10 μm from the exposed metal electrode) rises sharply, reaching 130 K under positive bipolar conditions and 200 K under negative bipolar conditions, respectively, further emphasizing the stronger thermal release intensity of negative polarity pulsed streamer.

Additionally, the generation and propagation of pressure waves during the streamer discharge is a characteristic feature of nSDBD, widely observed in experimental and numerical simulation studies.[55–58] The formation mechanism of these pressure waves is closely related to the spatial non-uniform distribution of gas temperature, which eventually evolves into radiating pressure waves as pressure accumulates. Figures 12(a) and 12(b) visually demonstrate the spatial structure of the pressure waves, including cylindrical pressure waves centered at the edge of the exposed electrode (appearing as semicircles in a 2D view) and planar pressure waves parallel to the dielectric surface. The cylindrical component originates from high-energy deposition at the electrode tip, while the planar wave is attributed to energy release within the discharge streamer. Negative bipolar pulses generate stronger planar pressure waves, consistent with previous studies,[24,25] indicating that for a given peak voltage and pulse energy, negative polarity pulsed streamers produce stronger pressure waves and more effectively couple electrical energy into the near-surface gas as heat,[22] making the temperature rise effect of negative bipolar pulse more significant. Notably, besides the positive pressure region at the wavefront, a negative pressure area also forms within the quarter-circle, further enriching the physical picture of nSDBD with this complex pressure distribution pattern.

IV. CONCLUSIONS

This paper systematically investigates atmospheric pressure air nSDBD through numerical simulations using a 2D fluid model. It thoroughly examines the impact of sinusoidal nanosecond pulse

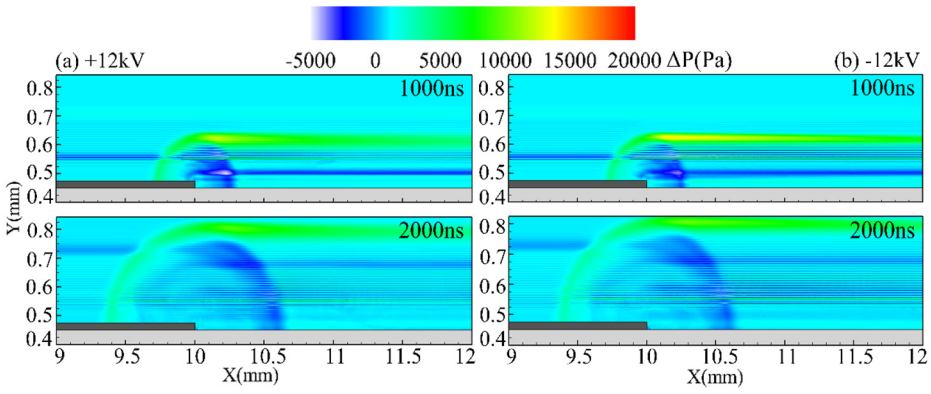

FIG. 12. (a) Positive and (b) negative bipolar pulsed pressure wave structure.

voltages of two polarities on nSDBD discharge characteristics, including discharge current, electron density distribution, electric field properties, surface charge evolution, energy density distribution, gas temperature, and pressure waves.

The results indicate significant differences in various discharge characteristics between positive and negative bipolar pulsed streamers, primarily stemming from their distinct discharge mechanisms. In terms of energy density distribution, the total deposited energy under the positive bipolar mode is significantly higher than that under the negative bipolar mode. However, the temperature rise induced by negative bipolar pulsed discharge around the electrodes is significantly higher than that of positive bipolar pulsed discharge. This phenomenon is attributed to the higher efficiency of negative bipolar pulsed streamers in converting electrical energy into thermal energy, which facilitates more effective coupling of thermal energy into the near-surface gas, resulting in a significant increase in local temperature. Moreover, the pressure waves generated by negative bipolar pulsed discharges are more intense, which can be attributed to their steeper gradient of gas temperature.

In summary, in-depth analysis of streamer discharges excited by positive and negative bipolar pulses reveals significant differences in discharge characteristics in terms of discharge current, particle density, surface charge distribution, energy density, gas temperature, and pressure waves. These research results provide important theoretical support for further optimizing nSDBD technology in applications such as air treatment, surface modification, and airflow control.

ACKNOWLEDGMENTS

This work was in part financially supported by the National Natural Science Foundation of China (Grant Nos. 12475261, 12065019, and 12405296). The authors would like to thank Dr. Chenhua Ren and Yifei Zhu for their helpful discussions.

AUTHOR DECLARATIONS

Conflict of Interest

The authors have no conflicts to disclose.

Author Contributions

Jiali Lai: Conceptualization (equal); Formal analysis (equal); Investigation (equal); Writing – original draft (lead). **Chunjing Wang:** Data curation (equal); Formal analysis (equal); Investigation (equal); Writing – original draft (equal). **Jing Li:** Data curation (equal); Investigation (equal); Methodology (equal); Writing – review & editing (equal). **Yi Peng:** Investigation (equal); Methodology (equal); Resources (equal); Writing – review & editing (equal). **Hancheng Xu:** Investigation (equal); Methodology (equal); Resources (equal); Writing – review & editing (equal). **Kaiyue Gao:** Data curation (supporting); Formal analysis (supporting); Resources (equal); Writing – review & editing (supporting). **Chuanjie Chen:** Formal analysis (supporting); Validation (lead); Writing – review & editing (supporting). **Muyang Qian:** Funding acquisition (equal); Project administration (equal); Software (equal); Supervision (equal). **Bingyan Dong:** Formal analysis (equal); Methodology (equal); Writing – review & editing (equal). **Dezhen Wang:** Data curation (lead); Writing – review & editing (equal).

DATA AVAILABILITY

The data that support the findings of this study are available from the corresponding authors upon reasonable request.

REFERENCES

[1]H.-H. Kim, Plasma Process. Polym. **1**, 91–110 (2004).
[2]S. Müller and R.-J. Zahn, Contrib. Plasma Phys. **47**, 520–529 (2007).
[3]M. Tański, A. Reza, D. Przytuła, and K. Garasz, Appl. Sci. **13**, 7001 (2023).
[4]S. B. Leonov, I. V. Adamovich, and V. R. Soloviev, Plasma Sources Sci. Technol. **25**, 063001 (2016).
[5]A. Y. Starikovskiy and N. L. Aleksandrov, Plasma Phys. Rep. **47**, 148–209 (2021).
[6]C. Zhang, B. Huang, Z. Luo, X. Che, P. Yan, and T. Shao, Plasma Sources Sci. Technol. **28**, 064001 (2019).
[7]N. A. Popov and S. M. Starikovskaia, Prog. Energy Combust. Sci. **91**, 100928 (2022).
[8]A. Starikovskiy and N. Aleksandrov, Prog. Energy Combust. Sci. **39**, 61–110 (2013).
[9]S. M. Starikovskaia, J. Phys. D: Appl. Phys. **47**, 353001 (2014).
[10]D. Opaits, D. Roupassov, S. Starikovskaia, A. Starikovskii, I. Zavialov, and S. Saddoughi, in 43rd AIAA Aerospace Sciences Meeting and Exhibit, Reno, NV, 2005.
[11]A. Y. Starikovskii, A. A. Nikipelov, M. M. Nudnova, and D. V. Roupassov, Plasma Sources Sci. Technol. **18**, 034015 (2009).
[12]I. N. Kosarev, V. I. Khorunzhenko, E. I. Mintoussov, P. N. Sagulenko, N. A. Popov, and S. M. Starikovskaia, Plasma Sources Sci. Technol. **21**, 045012 (2012).
[13]E. Moreau, J. Phys. D: Appl. Phys. **40**, 605 (2007).
[14]M. A. Boumehdi, S. A. Stepanyan, P. Desgroux, G. Vanhove, and S. M. Starikovskaia, Combust. Flame **162**, 1336–1349 (2015).
[15]E. M. Anokhin, D. N. Kuzmenko, S. V. Kindysheva, V. R. Soloviev, and N. L. Aleksandrov, Plasma Sources Sci. Technol. **24**, 045014 (2015).
[16]V. R. Solovev, A. M. Konchakov, V. M. Krivtsov, and N. L. Aleksandrov, Plasma Phys. Rep. **34**, 594–608 (2008).
[17]V. R. Soloviev and V. M. Krivtsov, Plasma Phys. Rep. **40**, 65–77 (2014).
[18]V. R. Soloviev, V. M. Krivtsov, S. A. Shcherbanev, and S. M. Starikovskaia, Plasma Sources Sci. Technol. **26**, 014001 (2016).
[19]T. C. Corke, C. L. Enloe, and S. P. Wilkinson, Annu. Rev. Fluid Mech. **42**, 505–529 (2010).
[20]J. Little, M. Nishihara, I. Adamovich, and M. Samimy, Exp. Fluids. **48**, 521–537 (2010).
[21]C. Ren, B. Huang, C. Zhang, B. Qi, W. Chen, and T. Shao, Plasma Sources Sci. Technol. **32**, 025004 (2023).
[22]R. Dawson and J. Little, J. Appl. Phys. **113**, 103302 (2013).
[23]N. Y. Babaeva, D. V. Tereshonok, and G. V. Naidis, Plasma Sources Sci. Technol. **25**, 044008 (2016).
[24]Y. Zhu and S. Starikovskaia, Plasma Sources Sci. Technol. **27**, 124007 (2018).
[25]J. Zhang, W. Tang, Y. Wang, and D. Wang, Plasma Sources Sci. Technol. **33**, 035004 (2024).
[26]S. A. Stepanyan, V. R. Soloviev, and S. M. Starikovskaia, J. Phys. D: Appl. Phys. **47**, 485201 (2014).
[27]S. A. Shcherbanev, S. A. Stepanyan, N. A. Popov, and S. M. Starikovskaia, Philos. Trans. R. Soc. A **373**, 20140342 (2015).
[28]S. A. Stepanyan, A. Y. Starikovskiy, N. A. Popov, and S. M. Starikovskaia, Plasma Sources Sci. Technol. **23**, 045003 (2014).
[29]B. Peng, N. Jiang, Y. Zhu, J. Li, and Y. Wu, Plasma Sources Sci. Technol. **33**, 045018 (2024).
[30]M.-Y. Qian, C.-S. Ren, D.-Z. Wang, Q.-Q. Fan, Q.-Y. Nie, X.-Q. Wen, and J.-L. Zhang, IEEE Trans. Plasma Sci. **40**, 1134–1141 (2012).
[31]S. A. Shcherbanev, A. Y. Khomenko, S. A. Stepanyan, N. A. Popov, and S. M. Starikovskaia, Plasma Sources Sci. Technol. **26**, 02LT01 (2016).
[32]C. Ding, A. Y. Khomenko, S. A. Shcherbanev, and S. M. Starikovskaia, Plasma Sources Sci. Technol. **28**, 085005 (2019).
[33]Q. Zhang, L. Zhang, D. Yang, J. Schulze, Y. Wang, and A. Bogaerts, Plasma Process Polym. **18**, 2000234 (2021).

[34]S. A. Shcherbanev, C. Ding, S. M. Starikovskaia, and N. A. Popov, Plasma Sources Sci. Technol. **28**, 065013 (2019).
[35]Y. Zhu, X. Chen, Y. Wu, and S. M. Starikovskaia, PASSKEy code, www.plasma-tech.net/parser/passkey/ (2021).
[36]G. J. M. Hagelaar and L. C. Pitchford, Plasma Sources Sci. Technol. **14**, 722 (2005).
[37]See www.lxcat.net for "SIGLO database."
[38]A. V. Phelps and L. C. Pitchford, Phys. Rev. A **31**, 2932 (1985).
[39]See www.lxcat.net for "PHELPS database."
[40]S. A. Lawton and A. V. Phelps, J. Chem. Phys. **69**, 1055–1068 (1978).
[41]G. V. Naidis, Plasma Sources Sci. Technol. **15**, 253 (2006).
[42]A. Bourdon, V. P. Pasko, N. Y. Liu, S. Célestin, P. Ségur, and E. Ségur, Plasma Sources Sci. Technol. **16**, 656 (2007).
[43]S. Pancheshnyi, Plasma Sources Sci. Technol. **24**, 015023 (2014).
[44]V. R. Soloviev and V. M. Krivtsov, Plasma Sources Sci. Technol. **27**, 114001 (2018).
[45]G. J. M. Hagelaar, F. J. De Hoog, and G. M. W. Kroesen, Phys. Rev. E **62**, 1452 (2000).
[46]N. A. Popov, J. Phys. D: Appl. Phys. **44**, 285201 (2011).
[47]S. Pancheshnyi, M. Nudnova, and A. Y. Starikovskii, Phys. Rev. E **71**, 016407 (2005).
[48]M. Capitelli, C. M. Ferreira, B. F. Gordiets, and A. I. Osipov, *Plasma Kinetics in Atmospheric Gases* (Springer Science & Business Media, 2001), Vol. 62, pp. 388–389.
[49]Y. Zhang, H. Wang, Y. Zhang, and A. Bogaerts, Plasma Sources Sci. Technol. **26**, 054002 (2017).
[50]N. Y. Babaeva and M. J. Kushner, Plasma Sources Sci. Technol. **18**, 035009 (2009).
[51]N. Y. Babaeva and M. J. Kushner, Plasma Sources Sci. Technol. **23**, 015007 (2014).
[52]J. Yao, J. Miao, J. Li, X. Lian, and J. Ouyang, Appl. Phys. Lett. **122**, 082905 (2023).
[53]Y. Zhu, S. Shcherbanev, B. Baron, and S. Starikovskaia, Plasma Sources Sci. Technol. **26**, 125004 (2017).
[54]C. Ren, B. Huang, J. Qiu, C. Zhang, B. Qi, W. Chen, and S. Shao, J. Phys. D: Appl. Phys. **55**, 235204 (2022).
[55]Y. Zhu, Y. Wu, W. Cui, Y. Li, and M. Jia, J. Phys. D: Appl. Phys. **46**, 355205 (2013).
[56]K. Takashima, Y. Zuzeek, W. R. Lempert, and I. V. Adamovich, Plasma Sources Sci. Technol. **20**, 055009 (2011).
[57]J. G. Zheng, Y. D. Cui, J. Li, and B. C. Khoo, Phys. Fluids **30**, 040907 (2018).
[58]F. Kong, Y. Wang, C. Zhang, X. Che, P. Yan, and T. Shao, Phys. Plasmas **24**, 123503 (2017).